Electrochimica Acta 220 (2016) 205–210

Contents lists available at ScienceDirect

Electrochimica Acta

journal homepage: www.elsevier.com/locate/electacta

Optimization of Lead-free Organic–inorganic Tin(II) Halide Perovskite Semiconductors by Scanning Electrochemical Microscopy

Hsien-Yi Hsu[a,1], Li Ji[a,b,1], Minshu Du[a], Ji Zhao[a], Edward T. Yu[b], Allen J. Bard[a,*]

[a] Center for Electrochemistry, Department of Chemistry, The University of Texas at Austin, Austin, TX 78712, United States
[b] Microelectronics Research Center, Department of Electrical and Computer Engineering, University of Texas at Austin, Austin, TX 78712, United States

ARTICLE INFO

Article history:
Received 5 August 2016
Received in revised form 28 September 2016
Accepted 8 October 2016
Available online 14 October 2016

Keywords:
non-toxic
lead-free
tin
perovskite
semiconductor
photoelectrochemistry
liquid junction
solar cell
scanning electrochemical microscopy

ABSTRACT

Lead-free organic-inorganic tin halide perovskites were prepared and investigated by a rapid screening technique utilizing a modified scanning electrochemical microscope (SECM). We studied liquid junction photoelectrochemical (PEC) solar cells based on p-type methylammonium tin halide ($MASnI_{3-x}Br_x$) perovskites employing the benzoquinone (BQ) redox couple, $BQ/BQ^{\bullet-}$, in dichloromethane (CH_2Cl_2). We found that the optimized Sn-based mixed halide perovskite, $MASnI_{0.5}Br_{2.5}$, exhibits enhanced performance and stability in liquid-junction PEC solar cells, with a power conversion efficiency of 1.51% (an increase of 20.8%) and a photovoltaic lifetime of 175 min (an increase of 75.0%), in comparison to $MASnI_3$ perovskites.

1. Introduction

Hybrid organic-inorganic perovskite materials have emerged as a new category of direct-bandgap semiconductors for solar energy applications. The impressive properties of perovskite materials, e.g., $MAPbX_3$ ($Me = CH_3$; X = I, Br, or Cl) for photovoltaic (PV) devices include very strong light absorption, excellent ambipolar charge mobility, small exciton binding energy, and apparent tolerance to defects [1–6]. The remarkably high power conversion efficiency (PCE) of 22.1% reported for hybrid Pb-based perovskite solar cells was achieved by optimizing both series resistance and band positions [7]. However, the most extensively explored hybrid perovskite materials contain the toxic metal lead, raising concerns about their environmental impacts. To replace Pb with a less toxic metal, Sn-containing compounds such as MASnI3 or $MASnI_{3-x}Br_x$ has been of considerable interest. Unfortunately, the Sn-containing materials are typically air and moisture sensitive, and their oxidation behavior can be detected in the evolution of powder diffraction patterns over time. The patterns show the appearance of extra Bragg diffraction peaks that belong to the oxidized Sn^{4+} species $(MA)_2SnI_6$, as determined by comparing the diffraction pattern of the unindexed peaks with those of Cs_2SnI_6 [8]. This process will destroy the charge neutrality of the perovskite structure and give rise to the formation of oxides/hydroxides of Sn and MAI. For solid-state lead free perovskite cells, the PCE of $MASnI_3$ can be further improved by partly substituting I with Br [9], although the solar energy efficiency of non-toxic tin-based perovskite photovoltaics is still low in comparison with lead-based perovskite solar cells. The photoluminescence decay lifetime and charge diffusion length for $MASnI_3$ solar cells were measured to be ~200 ps and 30 nm, respectively [10]. If the background doping level of $MASnI_3$ was controlled to be $10^{15}\,cm^{-3}$, however, the diffusion length would increase to 1 μm [10]. Given these developments, the determination of tin-based mixed halide perovskite compositions optimized for photovoltaic performance is of outstanding interest.

In a previous paper, we described liquid-junction PEC solar cells involving $MAPbI_3$ perovskites [5]. The $MAPbI_3$ perovskites are extremely sensitive to moisture[11] and unstable in polar solvents. We found that dichloromethane (CH_2Cl_2) can be used for liquid-junction PEC solar cells with reasonable stability because of its relatively higher dielectric constant [5]. Because the use of liquid electrolytes allows easy combinatorial synthesis and screening of new perovskite materials in arrays as well as testing of the effects of various dopants, we apply this solvent system with

* Corresponding author.
E-mail address: ajbard@mail.utexas.edu (A.J. Bard).
[1] These authors contributed equally.

http://dx.doi.org/10.1016/j.electacta.2016.10.049
0013-4686/

benzoquinone redox couples ($BQ/BQ^{\bullet-}$) to investigate tin-based mixed halide perovskites $MASnI_{3-x}Br_x$ using robotic synthesis and rapid screening based on scanning electrochemical microscopy, and to optimize compositions for photovoltaic performance.

2. Experimental section

2.1. Materials

Methylamine (MA, 2 M in methanol, Alfa Aesar), hydroiodic acid (HI, 57 wt.% in water, Alfa Aesar), methylammonium bromide tin iodide (MABr, 98%, Sigma-Aldrich), (SnI_2, 99.9985% metals basis, Alfa Aesar), tin bromide ($SnBr_2$, 99% metals basis, Alfa Aesar), N,N-Dimethylformamide (DMF, ≥99.9%, Sigma-Aldrich), Methylene chloride (CH_2Cl_2, anhydrous, ≥99.9%, Sigma-Aldrich), Tetrahydrofuran (THF, anhydrous, ≥99.9%, Sigma-Aldrich), Ethyl acetate (EA, anhydrous, ≥99.8%, Sigma-Aldrich), *p*-Benzoquinone (BQ, ≥99.5%, Sigma-Aldrich), Tetrabutyl-ammonium hexafluorophosphate ($TBAPF_6$, ≥99.9%, Sigma-Aldrich). FTO-coated glass was obtained from Pilkington (Toledo, OH) as a substrate of the electrodes. The 15 × 15 mm FTO-coated glass squares were cleaned by successive sonication in ethanol and 2-propanol and rinsed with deionized water.

2.2. Preparation of Perovskite Film

$MASnI_{3-x}Br_x$ was spin-cast on fluorine-doped tin oxide (FTO) glass substrates from N,N-dimethylformamide (DMF) (Alfa Aesar) solution with the mixture of MAI, MABr, SnI_2 and $SnBr_2$. MAI was synthesized by stirring 27.86 mL methylamine (2 M in methanol, Alfa Aesar) and 30 mL of hydroiodic acid (57 wt.% in water, Alfa Aesar) in a 250 mL round bottomed flask in an ice bath under an argon atmosphere for 3 hours. After the reaction, the solvent was evaporated using a rotary evaporator. A white powder, methyl ammonium iodide (MAI), was washed with diethyl ether by stirring the solution for 30 min, which was repeated three times, and then finally dried at 60 °C in vacuum oven for 24 h [12]. The synthesized MAI white powder was mixed with PbI_2 (Alfa Aesar) in DMF at 125 °C for one hour [13].

2.3. Preparation of Photocatalyst Spot Array Electrodes

Spot array electrodes (an electrode composed of spots with each spot having a different composition) were fabricated by a previously reported method [14,15] using a CH Instruments dispenser. The precursor solutions (0.518 M in DMF) were dispensed on the FTO substrate to create the spot array electrode. To accomplish this the piezo-dispensing tip was moved to a programmed position over the FTO substrate, and dispensing drops (~100 pL/drop) of the precursor solution. The tin halide precursor solution, SnI_2 and $SnBr_2$, was dispensed first in a preprogrammed pattern onto the FTO substrate, followed by the second precursor solution, MAI and MABr, dispensed onto the FTO in an overlay pattern. The distance between photocatalyst spots on the array was about 150 μm with a spot diameter of approximately 350 μm. Each spot had a total of 25 drops, and the spot composition is reported as the relative number of drops of each precursor solution. In all cases, the composition of $MASnI_{3-x}Br_x$ perovskites was controlled from the ratio of precursors. The prepared arrays were annealed at 125 °C for 1 h in air to form the $MASnI_{3-x}Br_x$ perovskites.

2.4. Screening of Spot Array Electrodes

A schematic SECM setup has been described previously [14,15]. Briefly, a 400 μm diameter optical fiber was connected to a 150 W xenon lamp (Oriel) and was attached to the tip holder of a CHI 900 B SECM. A 420 nm long-pass filter (removing the UV portion of the spectrum) was used for visible light only illumination in rapid screening experiments. The perovskite array was used as the working electrode and was placed in the bottom of a custom designed Teflon SECM cell with an O-ring (exposed area: 1.0 cm^2). A Pt wire was used as the counter electrode, and a saturated $Ag/AgNO_3$ electrode was used as the reference electrode. The electrolyte consisted of 2 mM BQ and 0.1 M $TBAPF_6$ (supporting electrolyte). Light from the xenon lamp was passed through the optical fiber, positioned perpendicular to the working electrode ~200 μm above the surface, to illuminate one spot on the working electrode at a time. The optical fiber tip was scanned across the spot array electrode with a scan rate of 500 μm/s, while a potential of −0.6 V vs $Ag/AgNO_3$ was applied to the working electrode through the SECM potentiostat. Scanning over the spot arrays revealed two-dimensional images indicative of the generation of photocurrent on each spot.

2.5. Photoelectrochemical measurements

The results on array electrodes were confirmed by PEC of perovskite films. The photoactivity of $MASnI_{3-x}Br_x$ was measured in a photoelectrochemical cell. The films were used as working electrodes (0.27 cm^2) exposed to electrolyte solution and irradiation. All measurements were carried out in a borosilicate glass cell with a carbon counter electrode and $Ag/AgNO_3$ reference electrode (a silver wire immersed in 0.01 M silver nitrate in MeCN connected to the cell via a 0.10 M $TBAPF_6$ in deaerated CH_2Cl_2 salt bridge) [5]. All potentials are reported vs. Fc/Fc^+ in deaerated CH_2Cl_2. The light source was irradiated through the electrolyte solution using full output of the Xe lamp with an incident light intensity of about 100 mW/cm^2. The supporting electrolyte was 0.1 M $TBAPF_6$ in deaerated CH_2Cl_2.

2.6. Instruments

A CH Instruments Model 760E electrochemical analyzer (Austin, TX) was used as a potentiostat for the experiments with the thin film electrodes. Illumination was with a Xenon lamp (XBO 150 W, Osram) at full output for UV–visible irradiation. Glancing incidence angle X-ray diffraction (XRD) measurements were performed by using D8 ADVANCE (Bruker, Fitchburg, WI) equipped with a Cu Kα radiation source where the incident angle was 0.4°. The film thickness was measured by scanning electron microscopy (SEM, Quanta 650 FEG, FEI Company, Inc., Hillsboro, OR). In the solar cell measurements, current (I) and voltage (V) readings were taken between the working electrode and the carbon counter electrode without external power source using a Keithley Model 2400 electrometer and a Xenon lamp solar simulator (Newport) equipped with an AM1.5G filter. For precursor dispensing, a CH Instruments model 1550 dispenser (Austin, TX) with a piezoelectric dispensing tip (Micro Jet AB-01-60, MicroFab, Plano, TX) connected to an XYZ stage driven by a computer-controlled stepper-motor system (Newport) was used.

3. Results and discussion

3.1. Current-Potential Behavior

Cyclic voltammograms (CVs) were measured for 2 mM BQ, 2 mM $BQ^{\bullet-}$ in 0.1 M $TBAPF_6$ at a glassy carbon electrode (diameter = 3 mm), displayed in Fig. 1a. This wave shows peak splitting with the first wave at − 0.90 V and the second at −0.70 V (formal potential = −0.80 vs. Fc/Fc^+). Under chopped illumination, a typical linear sweep voltammogram (LSV), as shown in Fig. 1b

exhibits demonstrates that a significant cathodic current flows with the onset at potentials negative by about 0.05 V vs. Fc/Fc^+, which should be near the perovskite valence band edge and correspond approximately to the flat band potential (E_{fb}). The photocurrent at potentials more positive than those for reduction at C electrode (Fig. 1a) represents conversion of radiant to electrical energy. The photocurrent density of p-$MASnI_3$ perovskite materials at −0.70 vs. Fc/Fc^+ is 0.9 mA/cm^2 with the fill factor of ~0.55. In comparison to tin-based perovskites, the photocurrent density and fill factor of $MAPbI_3$ perovskites are approximately 4.2 mA/cm^2 and 0.60, respectively. Fig. 1 shows that the difference, ΔE, between the onset potential for the photocurrent, E_{on}, and the standard potential of the redox couple, E^o, is 0.85 V. The individual current–potential behaviors of other $MASnI_{3-x}Br_x$ perovskites in a 2 mM $BQ^{\bullet-}$/BQ solution were also investigated, and onset potentials of their photocurrents are listed in Table 1.

Table 1
Flatband potential and onset Potential of Photocurrent.[a]

$MASnI_{3-x}Br_x$	E_{fb}, V	E_{on}, V vs. Fc/Fc^+	$\Delta E = E_{on} - E^o = E_{on} - (-0.8)$, V[b]
x = 0.0	0.06 ± 0.01	0.05	0.85
x = 0.5	0.09 ± 0.01	0.10	0.90
x = 1.0	0.13 ± 0.01	0.15	0.95
x = 1.5	0.21 ± 0.01	0.20	1.00
x = 2.0	0.25 ± 0.01	0.25	1.05
x = 2.5	0.28 ± 0.01	0.30	1.10
x = 3.0	0.33 ± 0.01	0.35	1.15

[a] The onset potential of photocurrent V_{on} here is defined as the potential at which 1% of the limiting or maximal photocurrent is observed.
[b] ΔE is the difference between the onset potential for the photocurrent, E_{on}, and the formal potential of the $BQ^{\bullet-}$/BQ redox couple, E^o, which is −0.8 V vs Fc/Fc^+.

3.2. Characterization of MASnI3-xBrx Perovskites

The $MASnI_{3-x}Br_x$ perovskite films were prepared by a one-step deposition and annealing process in a nitrogen glovebox. $MASnI_{3-x}Br_x$ was tuned by varying the content of bromide in the precursor solution. The compositions of $MASnI_{3-x}Br_x$ perovskite films were then characterized by X-ray diffraction (XRD) patterns. In Fig. 3, the diffraction pattern of $MASnI_3$ is seen to correspond well to simulated and literature data [8], and represents the tetragonal conformation of the perovskite structure [8]. Without doping any bromide, the structure of $MASnI_3$ is the same with that of methylammonium lead halide perovskites, $MAPbI_3$ [5,16]. In this case, the diffraction patterns demonstrate that the replacement of the central metal atom does not have an influence on the overall crystal structure of the material (Fig. 2). Because this series of $MASnI_{3-x}Br_x$ perovskites does not show any structural transitions at room temperature, they maintain the crystal structure of both end members, as given in Fig. 2.

3.3. SECM Scanning of Perovskite Arrays

A method for rapid screening of semiconductor materials by utilizing a form of the modified SECM has been reported previously [17]. Briefly, arrays composed of ~ 350-μm diameter semiconductor spots with different compositions were deposited by a piezoelectric dispenser onto a conductive fluorine-doped tin oxide (FTO) substrate. The scanning tip of the modified SECM was replaced by a 300 μm fiber optic connected to a xenon lamp and was rapidly scanned over the array. This combinatorial screening technique can reduce the effort and material expended in the optimization process [18,19], and offers rapid, automated evaluation of the photocurrent response at the substrate of different elements in the semiconductor array [15,20]. In this study, we performed a rapid screening analysis on $MASnI_{3-x}Br_x$ perovskite semiconductors with a modified SECM. The arrays contained three rows and seven columns of spots. To test the reproducibility, the first and second seven-spot rows are pristine $MASnI_3$ perovskites. The photocurrents of all 14 spots are nearly identical (~0.95 ± 0.2 μA). The third seven-spot row we analyzed is spot arrays of $MASnI_{3-x}Br_x$ perovskite materials with the value of x from 0 to 3. We observe that the photocurrent density of $MASnI_{3-x}Br_x$ perovskite materials decreases with increasing bromide content, consistent with previously reported results [9].

While it has been established that the maximum power conversion efficiency (PCE) of photovoltaic devices may be increased by introduction of bromide in $MASnI_3$ due to the larger open-circuit voltage [21], SECM rapid screening of $MASnI_{3-x}Br_x$ materials enables determination of the optimum amount of bromide in the $MASnI_{3-x}Br_x$ perovskite. Employing the SECM technique, we screened spot array electrodes to determine the dependence of photocurrent response on $MASnI_{3-x}Br_x$ perovskites with bromide content ranging from x = 0 to x = 3. The rapid screening results showed that $MASnI_3$ gave rise to the highest photocurrent (~0.95 μA) under irradiation. The photocurrent density decreases with increasing the content of bromide, as presented in Fig. 3, which shows a representative example of the SECM result of a $MASnI_{3-x}Br_x$ spot array electrode under

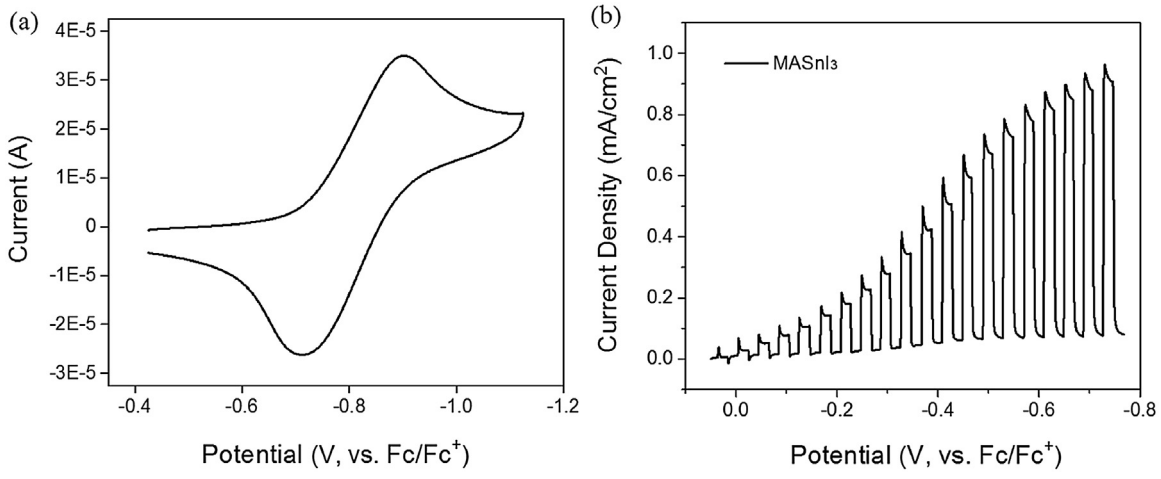

Fig. 1. Fig. 1. Voltammetric curves of p-$MASnI_3$ and C in CH_2Cl_2 containing 2 mM BQ, 2 mM $BQ^{\bullet-}$ and 0.1 M $TBAPF_6$ (supporting electrolyte). Light source, 100 mW/cm^2 xenon lamp. Scan rate = 50 mV/sec. (a) cyclic voltammogram at C electrodes (b) LSV characteristics under chopped illumination on p-$MASnI_3$ (b).

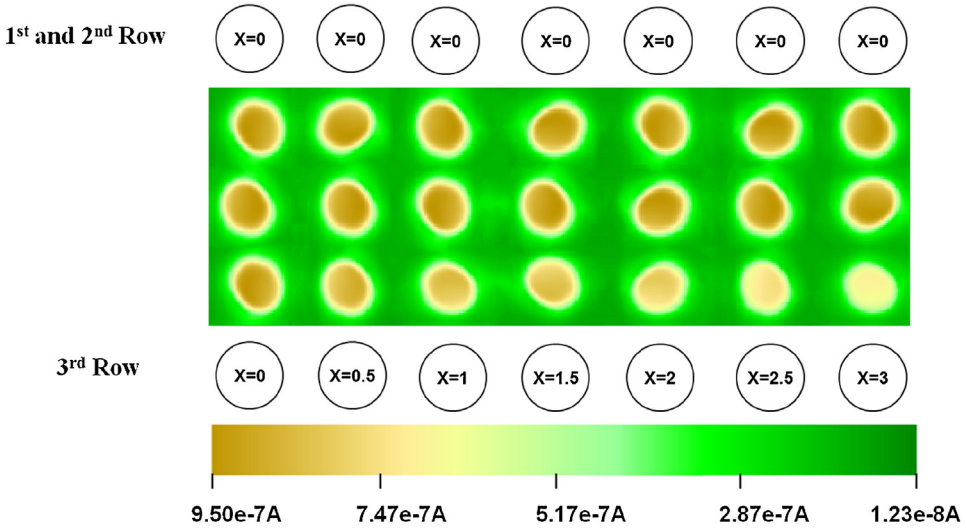

Fig. 3. SECM images for the absolute photocurrent of $MASnI_{3-x}Br_x$ perovskites under irradiation. The color represents the measured photocurrent shown in the scale bar below the SECM image. The first and second seven-spot rows are pure MASnI3 perovskites. The third seven-spot row represents $MASnI_{3-x}Br_x$ perovskite materials in each spot in the array electrode. The photocurrent shown is for 2 mM BQ reduction with 0.1 M $TBAPF_6$ supporting electrolytes in CH_2Cl_2 measured at an applied potential of −0.6 V vs Fc/Fc^+.

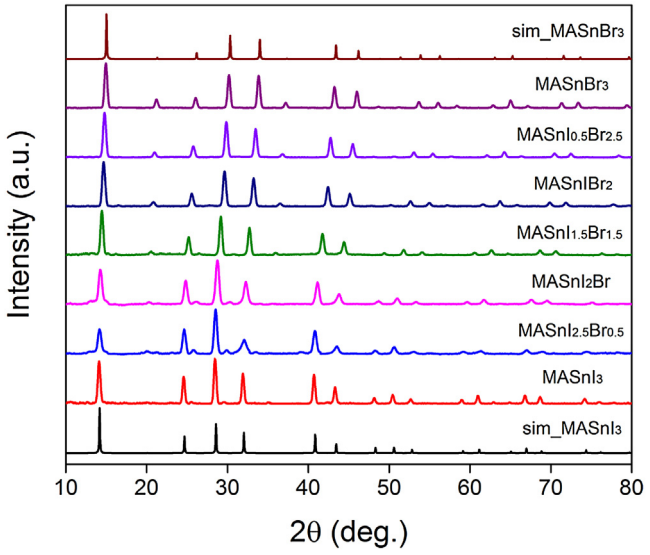

Fig. 2. X-ray diffraction patterns of $MASnI_{3-x}Br_x$ perovskite films with increasing content of bromide.

irradiation. The colors in Fig. 2 represent the photocurrent for BQ reduction at an applied potential of −0.6 V vs Fc/Fc^+ with browns representing higher currents and greens representing lower currents. The leftmost spot on third seven-spot row of the spot array represents pure $MASnI_3$, and then moving right, each spot has an increased bromide content in $MASnI_{3-x}Br_x$ perovskites, as shown by the schematic below the SECM image.

3.4. Capacitance Measurements

Determination of the energy levels of the semiconductor electrode with reference to the solution energy level is beneficial for maximizing the performance of a PEC solar cell. The valence band edge, E_v, and flat band potential, E_{fb}, can be determined by capacitance measurements (Mott-Schottky plots), i.e. capacitance of the semiconductor/electrolyte interface as a function of the applied potential. This capacitance is assumed to be the semiconductor space-charge capacitance, where E_{fb} can be estimated from the potential-axis intercept [22]. MS analysis of p-$MASnI_3$ electrode in CH_2Cl_2/0.1 M $TBAPF_6$ for frequencies of 500 Hz, 2 kHz, and 5 kHz are shown in Fig. 4. The x-intercepts of the solid lines indicate that E_{fb} appears to be ~0.06 ± 0.01 V vs Fc/Fc+, which is close to the onset photopotential of p-$MASnI_3$ in a $BQ^{\bullet-}$/BQ system (onset potential = 0.05 vs. Fc/Fc +). The MS plots for other $MASnI_{3-x}Br_x$ perovskite materials were also measured and their flatband potentials are displayed in Table 1. Clearly, E_{fb} is dependent on the content of bromide, and ΔE increases with increasing bromide content.

3.5. PEC solar cells

The LSV behavior can be used as a guide for the construction of PEC photovoltaic cells, where the open-circuit potential of the

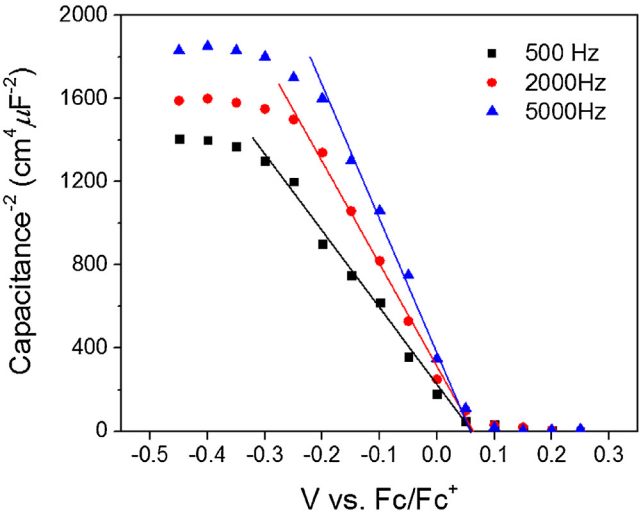

Fig. 4. Mott-Schottky plot of p-$MASnI_3$ in CH_2Cl_2 containing 0.1 M $TBAPF_6$ supporting electrolyte at 500 Hz, 2000 Hz, and 5000 Hz. The solid lines are linear fits to the experimental data.

semiconductor ideally (in the absence of recombination) approaches ΔE. The photocurrent responses found in the LSV experiments with $MASnI_{3-x}Br_x$ were recognizable, clearly indicating that the responses are not caused by conductivity changes under illumination. Thus, the experimental results between actual two-electrode photovoltaic cells are also of interest. The PEC behavior of these electrodes was investigated in a cell. The following cells were prepared: p-$MASnI_{3-x}Br_x/CH_2Cl_2$, $TBAPF_6$ (0.1 M), $BQ^{\bullet-}$ (2 mM), BQ (2 mM)/C (x = 0 to 3). The p-$MASnI_{3-x}Br_x$ photocathode and the reticulated vitreous carbon counter electrode were spaced apart with a Teflon gasket about 0.30 mm, with the p-$MASnI_{3-x}Br_x$ electrode about < 1 mm away from the cell window. To decrease the light adsorption by the intensely colored redox species, the $BQ^{\bullet-}$/BQ solutions were kept at a low concentration. The overall optical-to-electrical energy conversion efficiencies for p-$MASnI_{3-x}Br_x$ perovskite liquid-junction solar cells are summarized in Fig. 5. It is obvious that the $MASnI_{0.5}Br_{2.5}$ based PEC solar cell exhibits the highest efficiency. In Fig. 6, PEC photovoltaic cells, with configurations of p-$MASnI_{0.5}Br_{2.5}/CH_2Cl_2$, BQ (2 mM), $BQ^{\bullet-}$ (2 mM)/carbon and p-$MASnI_3/CH_2Cl_2$, BQ (2 mM), $BQ^{\bullet-}$ (2 mM)/carbon, show open-circuit photovoltages of 0.8 V and 0.7 V, as well as short-circuit current densities of 3.15 mA/cm^2 and 3.40 mA/cm^2 under 100 mW/cm^2 irradiation. The overall optical-to-electrical energy conversion efficiencies are 1.51% and 1.25%, respectively.

In addition, the photocurrent responses for the $MASnI_{0.5}Br_{2.5}$ and $MASnI_3$ in 2 mM $BQ^{\bullet-}$/BQ system were measured as a function of wavelength over the range 350 to 980 nm using a Xe lamp. The incident photon-to-electron conversion efficiencies (IPCEs) were calculated and are plotted in Fig. 7. For $MASnI_{0.5}Br_{2.5}$, it reaches a maximum of 39% at 445 nm and sharply declined at around 710 nm. The IPCEs of $MASnI_3$ perovskites moderately increased to 33% at 790 nm and then decreased at longer wavelength. Integration of the IPCE spectra for $MASnI_{0.5}Br_{2.5}$ and $MASnI_3$ perovskites gives current densities of 3.0 mA/cm^{2}and 3.5 mA/cm^2, in good agreement with the current densities measured using the solar simulator. The stability was monitored for unencapsulated p-$MASnI_{0.5}Br_{2.5}$ and p-$MASnI_3$ perovskite PEC solar cells in ambient atmosphere under irradiation at higher power intensity (150 mW/cm2), as shown in Fig. 8. The normalized efficiency for p-$MASnI_{0.5}Br_{2.5}$ perovskites is reduced by 70% for 120 min. However,

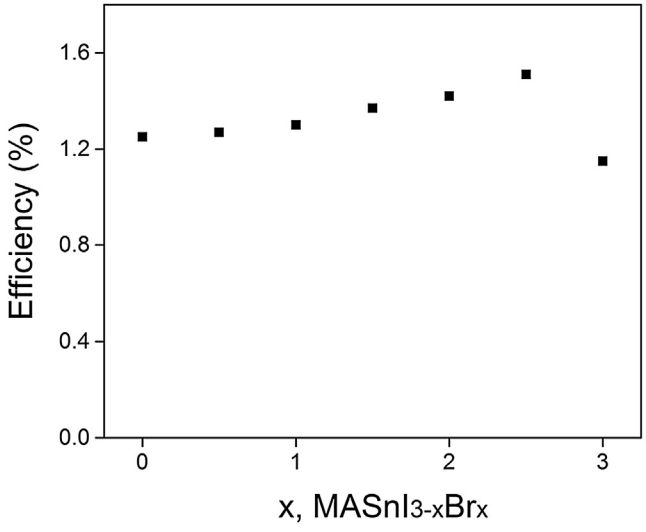

Fig. 5. Efficiencies of $MASnI_{3-x}Br_x$-based PEC solar cells under irradiation with a 100 mW/cm^2 xenon lamp focused onto the photoelectrode. The optical path through the solution was about 0.3 mm.

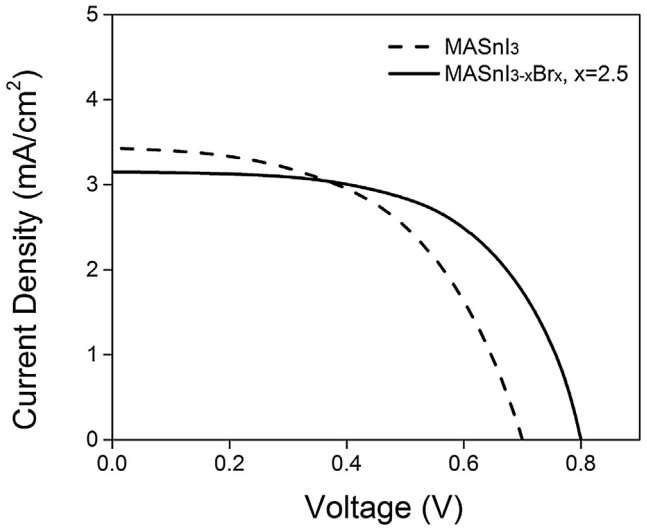

Fig. 6. Steady-state current density–voltage relation for p-$MASnI_{0.5}Br_{2.5}/CH_2Cl_2$, BQ (2 mM), $BQ^{\bullet-}$ (2 mM)/C and p-$MASnI_3/CH_2Cl_2$, BQ (2 mM), $BQ^{\bullet-}$ (2 mM)/C PEC solar cells under irradiation with a 100 mW/cm^2 xenon lamp focused onto the photoelectrode. The optical path through the solution was about 0.3 mm.

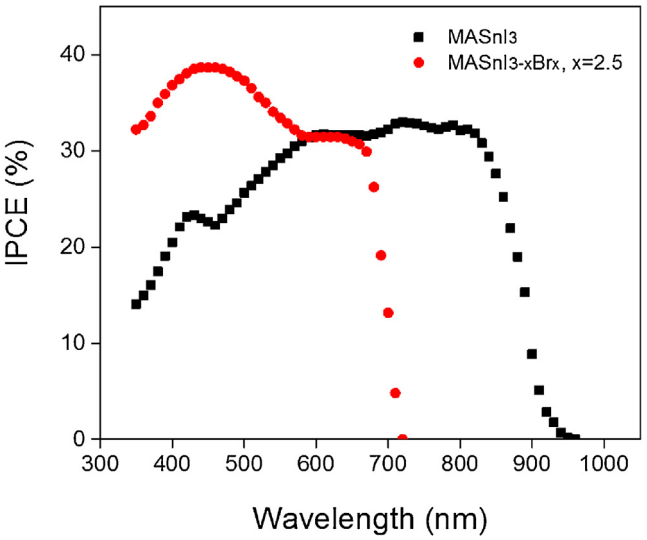

Fig. 7. IPCE spectra for p-$MASnI_{0.5}Br_{2.5}$ and p-$MASnI_3$ perovskite PEC solar cells.

p-$MASnI_3$-based PEC solar cells degraded completely within 100 min. We thus demonstrate that the $MASnI_{0.5}Br_{2.5}$ based solar cell shows improved stability compared to that for p-$MASnI_3$ perovskites.

4. Summary and conclusion

We have optimized p-type methylammonium tin halide ($MASnI_{3-x}Br_x$)-based liquid junction PEC solar cells by using a modified SECM imaging apparatus equipped with an optical fiber as a screening tip. We demonstrate that $MASnI_{0.5}Br_{2.5}$ shows higher solar cell efficiency and longer stability in a photoelectrode array system containing a series of $MASnI_{3-x}Br_x$ perovskite semiconductors on the FTO substrate. The PCE of liquid-junction solar cells is increased to the 1.51% as a result of the introduction of bromine. With regards to $MASnI_{0.5}Br_{2.5}$ perovskites, their lifetime is prolonged compared to that of $MASnI_3$-based devices.

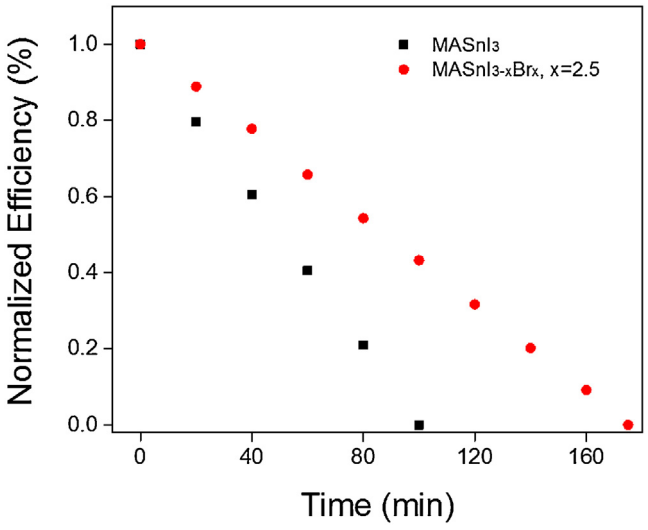

Fig. 8. Normalized efficiency of unencapsulated p-$MASnI_{0.5}Br_{2.5}$ and p-$MASnI_3$ perovskite PEC solar cells in ambient atmosphere. The $MASnI_{0.5}Br_{2.5}$ and p-$MASnI_3$ photoelectrodes was irradiated by a 150 mW/cm^2 Xe lamp. The optical path through the solution was about 0.3 mm.

Notes

The authors declare no competing financial interests.

Acknowledgements

The authors gratefully acknowledge the U.S. Department of Energy SISGR (DE-FG02-09ER16119) and the Robert A. Welch Foundation (F-0021).

Appendix A. Supplementary data

Supplementary data associated with this article can be found, in the online version, at http://dx.doi.org/10.1016/j.electacta.2016.10.049.

References

[1] L. Etgar, P. Gao, Z. Xue, Q. Peng, A.K. Chandiran, B. Liu, et al., Mesoscopic CH3NH3PbI3/TiO2 Heterojunction Solar Cells, Journal of the American Chemical Society 134 (2012) 17396–17399.
[2] C. Kagan, D. Mitzi, C. Dimitrakopoulos, Organic-inorganic hybrid materials as semiconducting channels in thin-film field-effect transistors, Science 286 (1999) 945–947.
[3] A. Kojima, M. Ikegami, K. Teshima, T. Miyasaka, Highly luminescent lead bromide perovskite nanoparticles synthesized with porous alumina media, Chemistry Letters 41 (2012) 397–399.
[4] P. Gao, M. Gratzel, M.K. Nazeeruddin, Organohalide lead perovskites for photovoltaic applications, Energy & Environmental Science 7 (2014) 2448–2463.
[5] H.-Y. Hsu, L. Ji, H.S. Ahn, J. Zhao, E.T. Yu, A.J. Bard, A Liquid Junction Photoelectrochemical Solar Cell Based on p-Type MeNH3PbI3 Perovskite with 1.05 V Open-Circuit Photovoltage. Journal of the American Chemical, Society 137 (2015) 14758–14764.
[6] H.-Y. Hsu, J.H. Vella, J.D. Myers, J. Xue, K.S. Schanze, Triplet Exciton Diffusion in Platinum Polyyne Films, The Journal of Physical Chemistry C 118 (2014) 24282–24289.
[7] Y. Zhou, K. Zhu, Perovskite Solar Cells Shine in the Valley of the Sun, ACS Energy Letters 1 (2016) 64–67.
[8] C.C. Stoumpos, C.D. Malliakas, M.G. Kanatzidis, Semiconducting tin and lead iodide perovskites with organic cations: phase transitions, high mobilities, and near-infrared photoluminescent properties, Inorganic chemistry 52 (2013) 9019–9038.
[9] F. Hao, C.C. Stoumpos, D.H. Cao, R.P. Chang, M.G. Kanatzidis, Lead-free solid-state organic-inorganic halide perovskite solar cells, Nature Photonics 8 (2014) 489–494.
[10] N.K. Noel, S.D. Stranks, A. Abate, C. Wehrenfennig, S. Guarnera, A.-A. Haghighirad, et al., Lead-free organic-inorganic tin halide perovskites for photovoltaic applications, Energy & Environmental Science 7 (2014) 3061–3068.
[11] G. Niu, X. Guo, L. Wang, Review of recent progress in chemical stability of perovskite solar cells, Journal of Materials Chemistry A 3 (2015) 8970–8980.
[12] J.-H. Im, C.-R. Lee, J.-W. Lee, S.-W. Park, N.-G. Park, 6.5% efficient perovskite quantum-dot-sensitized solar cell, Nanoscale 3 (2011) 4088–4093.
[13] Y. Zhao, K. Zhu, CH3NH3Cl-Assisted One-Step Solution Growth of CH3NH3PbI3: Structure, Charge-Carrier Dynamics, and Photovoltaic Properties of Perovskite Solar Cells, The Journal of Physical Chemistry C 118 (2014) 9412–9418.
[14] J. Lee, H. Ye, S. Pan, A.J. Bard, Screening of photocatalysts by scanning electrochemical microscopy, Analytical chemistry 80 (2008) 7445–7450.
[15] H.-Y. Hsu, L. Ji, M. Du, J. Zhao, E.T. Yu, A.J. Bard, Optimization of PbI2/MAPbI3 Perovskite Composites by Scanning Electrochemical Microscopy, The Journal of Physical Chemistry C 120 (2016) 19890–19895.
[16] M.M. Lee, J. Teuscher, T. Miyasaka, T.N. Murakami, H.J. Snaith, Efficient hybrid solar cells based on meso-superstructured organometal halide perovskites, Science 338 (2012) 643–647.
[17] J.L. Fernández, N. Mano, A. Heller, A.J. Bard, Optimization Of Wired Enzyme O2-Electroreduction Catalyst Compositions by Scanning Electrochemical Microscopy, Angewandte Chemie 116 (2004) 6515–6517.
[18] J.L. Fernández, N. Mano, A. Heller, A.J. Bard, Optimization Of Wired Enzyme O2-Electroreduction Catalyst Compositions by Scanning Electrochemical Microscopy, Angewandte Chemie International Edition 43 (2004) 6355–6357.
[19] N. Mano, H.-H. Kim, A. Heller, On the relationship between the characteristics of bilirubin oxidases and O2 cathodes based on their wiring, The Journal of Physical Chemistry B 106 (2002) 8842–8848.
[20] F. Hao, C.C. Stoumpos, R.P. Chang, M.G. Kanatzidis, Anomalous band gap behavior in mixed Sn and Pb perovskites enables broadening of absorption spectrum in solar cells, Journal of the American Chemical Society 136 (2014) 8094–8099.
[21] L. Wang, C. McCleese, A. Kovalsky, Y. Zhao, C. Burda, Femtosecond Time-Resolved Transient Absorption Spectroscopy of CH3NH3PbI3 Perovskite Films: Evidence for Passivation Effect of PbI2, Journal of the American Chemical Society 136 (2014) 12205–12208.
[22] G. Nagasubramanian, A.S. Gioda, A.J. Bard, Semiconductor Electrodes XXXVII. Photoelectrochemical Behavior of p-Type in Acetonitrile Solutions, Journal of the Electrochemical Society 128 (1981) 2158–2164.